PNAS Nexus, 2026, **5**, pgag077
https://doi.org/10.1093/pnasnexus/pgag077
Published: 25 March 2026
Research report

Measurement-induced phase transitions in informational active matter

Bryan VanSaders[1,5], Michel Fruchart[2], and Vincenzo Vitelli[1,3,4]*

[1]James Franck Institute, The University of Chicago, Chicago, IL 60637, USA
[2]Gulliver, ESPCI Paris, Université PSL, CNRS, Paris 75005, France
[3]Department of Physics, The University of Chicago, Chicago, IL 60637, USA
[4]Kadanoff Center for Theoretical Physics, The University of Chicago, Chicago, IL 60637, USA
[5]Present address: Department of Physics, Drexel University, Philadelphia, PA 19104, USA.
*To whom correspondence should be addressed: Email: vitelli@uchicago.edu
Edited By Derek Abbott

Abstract

Various biological and synthetic media out of equilibrium can be viewed as many-ratchet systems that rectify environmental noise through local measurements and information processing, like Maxwell's prototypical demon. These systems pose a challenge to standard coarse-graining approaches because they are described in terms of decision-making protocols similar to computer programs rather than force laws. Here, we study a many-body generalization of the Maxwell demon problem: a fluid composed of adaptive particles that achieve collective behavior by biasing noise-driven scattering events subject to measurements. Using a combination of information-theoretic, kinetic, and hydrodynamic tools, we elucidate how microscopic decision-making protocols, rather than microscopic forces, generate macroscopic active states sustained by continuous measurements. These include an informational version of flocking whose order parameter is bounded by the information measured, and the onset of which may be viewed as a measurement-induced phase transition. We find that the signature of such microscopic choices is an "informational activity" that selectively compresses phase space, without work, and causes deviations from equilibrium scaling with the magnitude of environmental noise. We envision applications to noise-induced patterning performed by collections of microrobots guided by reinforcement learning or programmable phoretic colloids in turbulent flows that exploit local measurements and control actions to counteract the scrambling of information by chaos.

Keywords active matter, flocking, reinforcement learning, information engines, measurement-induced phase transitions

Significance statement

Biological and synthetic systems that sense and react to their noisy environments can operate like ratchets, selectively "opting out" of interactions to pursue a goal. When these optional interactions happen between agents in a large collective, group behavior emerges from many local measurements and decisions. Here, we construct a model hard sphere fluid and demonstrate how local information processing drives nonequilibrium collective states, including an informationally driven version of flocking, whose onset can be viewed as a measurement-induced phase transition. We find that such "informational" activity generically increases as noise grows, even for nonthermal noise sources. Our work advances understanding of decision-based collective behavior in situations where groups of information processing agents contend with intense noise, ranging from thermal fluctuations at nanoscopic scales to granular vibrations and turbulent flows.

Received: September 17, 2025. **Accepted:** February 4, 2026
© The Author(s) 2026. Published by Oxford University Press on behalf of National Academy of Sciences.
This is an Open Access article distributed under the terms of the Creative Commons Attribution-NonCommercial License (https://creativecommons.org/licenses/by-nc/4.0/), which permits non-commercial re-use, distribution, and reproduction in any medium, provided the original work is properly cited. For commercial re-use, please contact reprints@oup.com for reprints and translation rights for reprints. All other permissions can be obtained through our RightsLink service via the Permissions link on the article page on our site—for further information please contact journals.permissions@oup.com.

Downloaded from academic.oup.com/pnasnexus/article/5/4/pgag077/8540115 by guest on 04 November 2026

Introduction

A macromolecular machine within a cell and a boat on troubled waters are both subject to relentless random forces driving chaotic dynamics: thermal fluctuations in the cell, waves and wind on the sea. At first sight, these strong fluctuations seem to be a challenge opposing the molecular machine's or boat's goals. However, both sailors and biological components can exploit noise for their own purposes by sensing their environment, taking actions informed by local measurements, and breaking time-reversal symmetry. This process turns them into "information engines" (1–6). Information engines operate not by applying forces but rather by restricting the volume of phase space available to the system through measurements. This excluded volume effect leads to entropic forces whose strength is proportional to temperature in a thermal system (7–13), like the pressure in an ideal gas (9), elasticity in rubber (14), or the phoretic forces underlying self-propelled colloids (15–18). Crucially, information engines can *actively* change the excluded volume in phase space depending on their state, setting up a feedback mechanism that drives the system out of equilibrium by rectifying noise and chaotic dynamics into a desired motion or behavior through local measurements and information processing (5, 19). This mechanism is believed to play a key role in biological and behavioral processes (7, 8, 20–35).

Considerable research has focused on single-body information engines, in which a lone agent (colloquially known as a Maxwell demon) exploits information as a resource to perform work toward a goal. However, theoretical descriptions of many-body information engines are comparatively rare (36–38). Many natural systems are composed of large numbers of cooperating agents that individually collect, process, and act on information (eg cells in a tissue, ant colonies, bird flocks, and human communities). Furthermore, over the last two decades, per-particle external feedback control has been demonstrated in synthetic active matter systems, such as programmable phoretic colloids (39–50). As colloidal scale objects are engineered to be more complex (51) and robotic platforms shrunk toward the colloidal regime (52, 53), a new category of small-but-capable machines are emerging (54–56). Yet, little is known about collective phenomena that arise in such many-body systems as a result of their ability to perform local measurements and control actions. We henceforth refer to these many-body systems as informational active matter. In this class of systems, measurements and control actions can counteract the scrambling of information by the underlying chaotic dynamics (eg microscopic collisions). As a consequence, this information, typically encoded in low-entropy ordered states, can survive in a nonequilibrium steady state.

To distill the nonequilibrium collective effects that arise purely from informational activity, we introduce a minimal extension of what is perhaps the simplest interacting many-body system, the hard disk gas. This extension, amenable to theoretical treatment, explicitly accounts for the feedback control processes whereby each agent (ie Maxwell demon) makes control decisions informed by the outcome of measurements. Such a gas of Maxwell demons can reach through consensus (but without exerting any work) a nematic flocking-like state that we analyze, from kinetic to hydrodynamic theory, by coarse-graining microscopic decision-making policies informed by measurements, rather than predetermined microscopic forces. We show that the steady-state magnitude of the nematic-flocking order parameter is bounded by the information measured, which suggests viewing the onset of informational flocking as a phase transition induced by measurements (57–61). This classical mechanism is reminiscent of quantum measurement-induced phase transitions (MIPT), where quantum measurements counteract the scrambling of information originating from the underlying unitary dynamics (62–64).

The demon gas model

Consider a gas of hard disks at finite temperature, undergoing random collisions with each other. The velocities of individual particles follow the Maxwell–Boltzmann (MB) distribution. Imagine now that these disks could "opt out" of collisions with other disks: this would allow them to select whatever velocity is desired by simply waiting until they obtain it randomly by collision, then subsequently avoiding scattering interactions. Such a system would act as a distributed version of the demon imagined by Maxwell, that opens and closes a trapdoor to create a temperature difference between two sides of a vessel filled with gas (3, 27, 65–68).

Here, we implement such a demon gas by endowing every disk in the gas with the ability to change its size, and therefore its scattering cross-section, depending on its environment. As shown in Fig. 1a, every period t_m, every particle i measures its current state (position $\boldsymbol{x}^{(i)}$ and velocity $\boldsymbol{v}^{(i)}$) as well as its environment $\mathcal{E}^{(i)}$ (ie some set of information about the current state of nearby particles). Based on these data, it changes its size according to a choice function $D(\boldsymbol{x}^{(i)}, \boldsymbol{v}^{(i)}, \mathcal{E}^{(i)})$ giving the new diameter of the particle.

In order to bring the informational aspects to the fore, we focus on the less explored limit where the functions D do not result in particles exerting work on each other. In most experimental contexts, the informational (ie entropic) effects highlighted here will generally coexist with active forces of enthalpic origin on which active matter theories typically focus (40–42, 44, 48, 50, 51). In the limit of vanishing work, size changes are confined to the times between collisions, ie when such a change would not cause overlaps (Fig. 1b), requiring that $\mathcal{E}^{(i)}$ provides proximity information about neighbors. As a consequence, the quantities conserved in a standard hard disk gas (mass, linear momentum, and total kinetic energy) are also conserved in the demon gas (see SI Sections S1 and S2).

Nonetheless, coupling particle size and velocity drives the system out of equilibrium, as shown in Fig. 1c. Crucially, collisions are no longer "undone" by reversing particle velocities if sizes also change, and hence detailed balance is broken (a hallmark of active systems but here achieved with energy and momentum conservation intact). As we now show, specifying the choice function D allows us to control the behavior of the fluid.

Informational flocking

We start by implementing an informational version of flocking. Flocking is typically modeled as arising from interaction torques that bring the orientations of self-propelled particles into alignment. No such forces are present in our model. Instead, flocking is produced by control actions whereby the particles simply align their velocities with their neighbors by selectively reducing their size when they are aligned and increasing their size when they are not aligned. These control actions are *local*, in the sense that the particles (agents) need not know their global positions. Over many collision

Downloaded from academic.oup.com/pnasnexus/article/5/4/pgag077/8540115 by guest on 04 November 2026

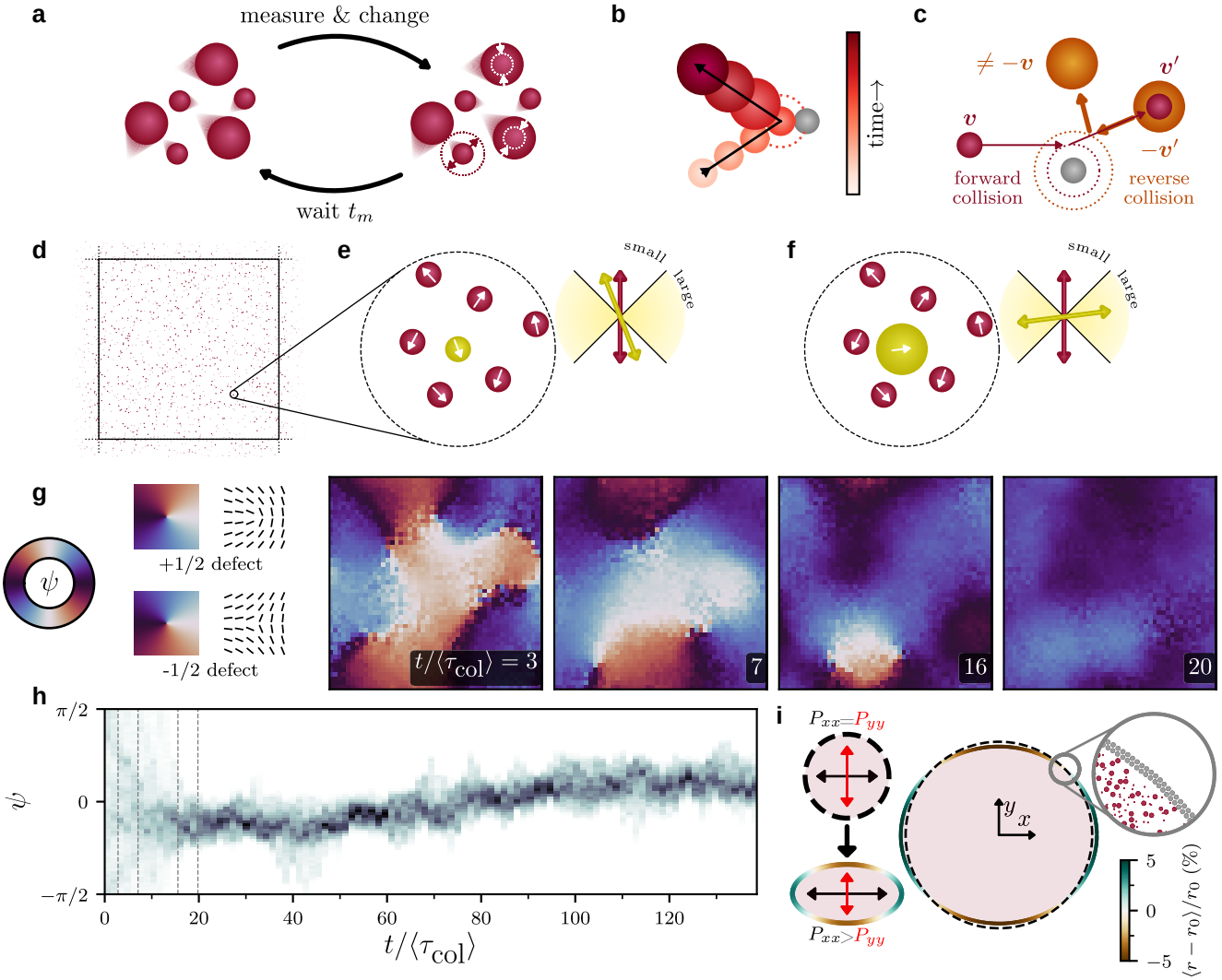

Figure 1 The demon gas uses measurement to break detailed balance without work. a) A gas of feedback controllers, hard disks capable of changing their diameter in response to a measurement. Here, we consider gases where measurements are instantaneous and synchronized, with a delay of t_m between subsequent measurements. b) Controllers maintain energy conservation during collision events by disallowing diameter changes that would introduce particle overlaps. c) Diameter as a function of particle velocity breaks detailed balance—a "reverse" collision that begins where a "forward" collision ends does not recover the initial configuration of the forward collision. d) A demon gas with periodic boundary conditions, simulated via molecular dynamics. e, f) Diameter changing conditions for a nematically aligning demon gas. e) When particle velocity is aligned (or antialigned) with the majority of nearby neighbors, a small diameter is chosen. f) When particle velocity is perpendicular to the majority of nearby neighbors, a large diameter is chosen. g) Snapshots of binned orientation fields for an initially passive gas at short times after diameter rescaling is enabled. $\langle\tau_{\rm col}\rangle$ is the mean collision time assuming an even split of large and small diameter particles. Nematic defects form and annihilate leading to a nearly uniform orientation. h) Long-time distribution of particle orientations for the gas in part (g). The times corresponding to snapshots in (g) are indicated with dashed lines. i) The anisotropic pressure of a demon gas trapped within a passive flexible container inflates it into an ellipsoidal shape (colored by radial deformation r from circular initial condition r_0).

events, this selective biasing of scattering cross-section results in aligned groups. As the total linear momentum is conserved, it is not possible to change the average velocity in the system (see below for a variant where this constraint is lifted), so we have a nematic version of flocking in which particles tend to align their velocities $\boldsymbol{v}^{(i)}$ modulo reflection $\boldsymbol{v}^{(i)} \to -\boldsymbol{v}^{(i)}$. This is represented in Fig. 1d–f: the current particle (centered) computes the average direction of neighboring particles and compares it to its own. Depending on whether the double-sided arrows are aligned or not (white and shaded regions in Fig. 1e, f), the particle adopts (between collisions) a small diameter $D_{\rm S}$ or a large diameter $D_{\rm L}$. Each particle takes a diameter $D(\theta) = D_{\rm S} + \Delta D\mathcal{H}(\cos^2\theta - 1/2)$, where $\mathcal{H}$ is the Heaviside step function, $\Delta D = D_{\rm L} - D_{\rm S} \geq 0$ is the diameter difference, and θ is the angle between the particle's direction of motion and the local average direction of motion in a region of volume Ω around the current particle (Fig. 1e, f). Formally, the average direction of motion is determined as the major axis of the local pressure tensor $P_{ij} = -\rho\langle p_i p_j\rangle_\Omega$, in which $\boldsymbol{p} \equiv \boldsymbol{v} - \boldsymbol{u}_\Omega$, $\boldsymbol{u}_\Omega \equiv \langle\boldsymbol{v}\rangle_\Omega$, and ρ is the gas density. Indeed, the traceless part $Q_{ij} = P_{ij} - (P_{kk}/d)\delta_{ij}$ of the (symmetric) pressure tensor can be interpreted as a nematic order parameter and decomposed as $Q_{ij} = 2Q[n_i(\psi)n_j(\psi) - \delta_{ij}/d]$ where d is the space dimension, $\hat{n}(\psi)$ is a unit vector making an angle ψ with a fixed direction (eg the x axis), and $Q^2 \equiv \|\boldsymbol{Q}\|^2 \equiv Q_{ij}Q_{ji}/2 \geq 0$. Note that here, the symmetric traceless tensor $\boldsymbol{Q}$ describes the motion of the particles, in contrast with nematic liquid crystals where the nematic tensor describes their orientation.

Figure 1g, h shows the result of molecular dynamics (MD) simulations of this model with periodic boundary conditions (see

Downloaded from academic.oup.com/pnasnexus/article/5/4/pgag077/8540115 by guest on 04 November 2026

Materials and methods and SI Section S1 for details). We observe that the gas acquires a finite nematic order parameter $\boldsymbol{Q}$ starting from a disordered initial configuration (the equilibrium state of the passive gas) as the rotation symmetry of the system is spontaneously broken, see Fig. 1g for a plot of the local orientation $\psi = \arctan(Q_{12}, Q_{11})/2$ (modulo π) and Fig. 1h for the time evolution of the histogram of ψ. Nematic defects in the orientation field eventually relax by annihilation (Fig. 1g), leaving the system with a single dominant (but thermally fluctuating) orientation. Note that these simulations are too small to prove the emergence of true global orientational order (69, 70) (see SI Section S3), and we leave the development of a fluctuation theory and accompanying scaling simulations to future work.

This alignment is accompanied by a stable anisotropy in the system-wide pressure tensor. Fixed diameter disks, in contrast, can only exhibit an isotropic pressure tensor. This ability can be harnessed to perform work. For instance, the gas can asymmetrically inflate a symmetric balloon, as shown in Fig. 1i. The resulting ellipsoidal shape of the balloon arises from the interplay between its surface tension (that favors a symmetric shape) and the nonequilibrium anisotropic pressure tensor of the gas (that favors an asymmetric shape). Such a mechanism could for instance be exploited to actuate a synthetic membrane from the inside.

Thermodynamics of information-driven fluids

In order to understand how the model in Fig. 1 harnesses information to maintain a nonequilibrium steady state and to perform work on a load, we turn to the framework of information thermodynamics (5, 71–73). In a nutshell, this framework provides a formulation of the second law of thermodynamics that integrates the fact that the entropy of a system can be reduced by acquiring information about it, and subsequently driven out of equilibrium by using control actions conditioned on the measurement results. To do so, one first introduces the nonequilibrium free energy $\mathcal{F}[\rho] = \langle U \rangle_\rho - TS[\rho]$ associated to a (possibly nonequilibrium) statistical state represented by a probability distribution ρ, where $\langle U \rangle_\rho$ is the mean internal energy in this state and $S[\rho]$ the entropy of the distribution. In general, the joint distribution of all measured variables must be considered to compute entropy. Here, we restrict ourselves to the single-particle velocity distribution function (a mean field approximation assuming that the alignment of a local neighborhood changes much slower than the individual velocities within it). In terms of these quantities, our assumption that the particles are not permitted to exert work on each other means that the mean internal energy $\langle U \rangle_\rho$ is constant. The second law of thermodynamics for feedback processes then states that the change $\Delta\mathcal{F}$ between two states satisfies (5, 72)

$$\Delta\mathcal{F} \leq W + k_B T I, \tag{1}$$

where W is the work done on the system during the process, and I the mutual information between the microstates of the system and the results of the measurements used for the feedback control.

The quantity $k_B I$ corresponds to the entropy reduction due to the control actions. The mutual information I can easily be computed in simple situations, but in general its evaluation is a challenging task, in particular because of correlations between successive measurements (5, 71, 72, 74, 75). In our case, all measurements are synchronized (Fig. 2a), but they take time to influence observable gas properties, because their consequences are only felt during collisions. Hence, their effect is smeared out over the average time between collisions τ_{col}. Once a particle has collided, its previous measurement becomes outdated because it may have changed direction, so the next collision will tend to equilibrate the gas. After a few τ_{col}, we expect the system to behave like an equilibrium hard disk gas until the next measurement. Figure 2b shows the reduction in entropy relative to the MB distribution $S - S^{\text{MB}}$ over time for $t_m \gg \tau_{\text{col}}$, showing successive dips in the entropy followed by a relaxation to equilibrium. Note that energy conservation implies that $\mathcal{F} - \mathcal{F}^{\text{MB}} = -T(S - S^{\text{MB}})$. In Fig. 2c, t_m is reduced, and the peaks corresponding to entropy dips are less and less pronounced until a stationary balance between entropy reduction and relaxation toward thermodynamic equilibrium is observed (blue curves). When $t_m \lesssim \tau_{\text{col}}$, the system does not fully relax to the equilibrium MB state, inducing correlations between subsequent measurements.

In order to assess the effect of measurements, we therefore take a phenomenological approach that captures the unidirectional coupling between the information-carrying degree of freedom (the particle diameters) and the velocities of the particles. We model the effect of each measurement as an instantaneous change of the free energy $\mathcal{F}_{\text{ic}}$ of the information carriers by a value $\mathcal{F}_{\text{m}}$, which takes place every t_m. The free energy stored in the diameters is purely informational (entropic). It relaxes to its equilibrium (MB) value $\mathcal{F}_{\text{ic}}^{\text{MB}}$ through collisions over a relaxation timescale τ, each time it is used to make a decision, and this leads to an equal increase in the free energy $\mathcal{F}$ associated with the velocities of the particles. Finally, $\mathcal{F}$ also relaxes to its equilibrium value $\mathcal{F}^{\text{MB}}$ with the same collisional time scale τ, in the same way as in a normal hard disk gas. This translates into the equations of motion

$$\dot{\mathcal{F}}_{\text{ic}} = -\frac{1}{\tau}[\mathcal{F}_{\text{ic}} - \mathcal{F}_{\text{ic}}^{\text{MB}}] + \mathcal{F}_{\text{m}} \text{Ш}_{t_m}(t) \tag{2a}$$

and

$$\dot{\mathcal{F}} = -\dot{\mathcal{F}}_{\text{ic}} - \frac{1}{\tau}[\mathcal{F} - \mathcal{F}^{\text{MB}}] \tag{2b}$$

in which Ш_{t_m} represents a series of unit impulse trains spaced by t_m. In the steady state, the departure $\Delta\mathcal{F}^*$ of $\mathcal{F}$ from the MB value just before a measurement does not change from a period to the next and one can show that $\Delta\mathcal{F}^* \propto \mathcal{F}_{\text{m}}$.[a] Fitting to numerical free energy data shown in Fig. 2c provides estimates of the parameters $\mathcal{F}_m$ and τ (see Fig. S1 in SI Section S1).

To estimate the amount of information collected by the disks, we describe the binary choice by a two-state Markov process, where the two states correspond to the two possible sizes a particle can take (see SI Section S1 for detailed methods). This neglects correlations between particles but captures correlations between successive measurements. The transition probabilities T_{ij} and steady-state distribution μ_i of the Markov chain are estimated from the numerical simulations, yielding the mean information per step as (54, 71, 76),

$$I \gtrsim I_{\text{MC}} \equiv -\sum_{ij} \mu_i T_{ij} \ln T_{ij}. \tag{3}$$

Downloaded from academic.oup.com/pnasnexus/article/5/4/pgag077/8540115 by guest on 04 November 2026

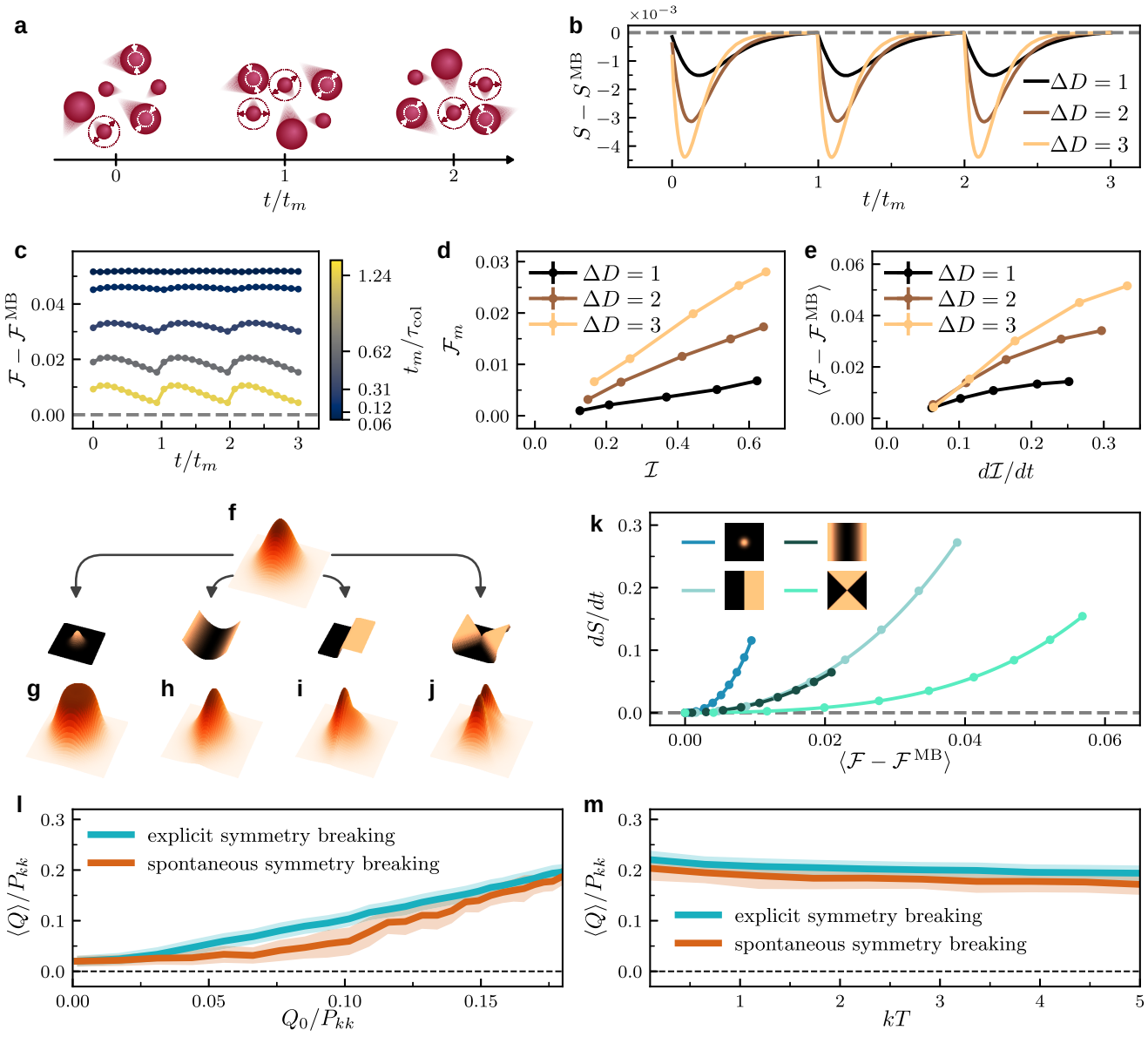

Figure 2 The demon gas is driven by information. a) Particles instantaneously measure their velocity and update their diameters (subject to constraints due to proximity) at an interval of t_m. b) The entropy (relative to the MB distribution) of a demon gas measured from its velocity distribution function. Here, the measurement interval is several times longer than the mean collision time ($t_m/\tau_{\mathrm{col}} = [3.6, 4.3, 5]$ for $\Delta D = [1, 2, 3]$). c) Relative entropy of demon gases with a range of measurement intervals, up to approximately one collision time. d) The nonequilibrium free energy injected at each measurement, as estimated by fitting curves similar to (c) as a function of the information per measurement of a Markov process describing the diameter of particles (see SI Fig. S1). Note that I increases with the interval between measurements t_m. The curves are always well below the diagonal. e) The average nonequilibrium free energy as a function of the information rate of the diameter Markov process. Note that for the values studied here dI/dt increases as t_m is reduced. f–j) The result of various diameter functions on the gas velocity distribution. f) The MB distribution in the velocity plane (constant diameter). g) A zero-centered Gaussian diameter function. h) A quadratic diameter function of one velocity component. i) A diameter step function that breaks reflection symmetry. j) A diameter step function in angular velocity coordinates that breaks pressure symmetry. k) The entropy production rate of various demon gases as a function of nonequilibrium free energy. l) Growth of the nematic order parameter with Q_0 for simulations of demon gases with explicitly and spontaneously broken symmetry. The system-wide average of the order parameter does not approach zero as $Q_0 \to 0$ due to thermal fluctuations. m) Nematic order parameter as temperature is increased 50-fold. Nematic ordering is approximately independent of temperature.

Strictly speaking, this is only a lower bound on the total information per step I. The results are shown in Fig. 2d, where we observe that the free energy impulses $\mathcal{F}_m$ scale with and remain bounded by the Markov estimate of information gained per measurement.

Due to correlations between measurements the amount of information gained per measurement decreases when $t_m < \tau_{\mathrm{col}}$. However, the average nonequilibrium free energy $\langle \mathcal{F} - \mathcal{F}^{\mathrm{MB}} \rangle$ increases with the rate of information acquisition (ie for rapid correlated measurements). For values of t_m studied here, increasing the rate of measurement increased dI/dt (ie correlations do not entirely negate the advantage of more rapid acquisition). Figure 2e shows that average nonequilibrium free energy scales with the rate of information gain. Overall, a larger diameter contrast ΔD leads to a larger effect (Fig. 2b, d, and e), while measurement time determines the mean and excursion of $\mathcal{F} - \mathcal{F}^{\mathrm{MB}}$.

Downloaded from academic.oup.com/pnasnexus/article/5/4/pgag077/8540115 by guest on 04 November 2026

Similar arguments can be used to obtain estimates of free energy expenditure in the case of a single demon particle immersed in a passive thermalized gas, see SI Section S4.

By analogy with Eq. 1, we expect $\Delta\mathcal{F}^* \propto \mathcal{F}_m \leq k_B T I$. This bound on the deviation from equilibrium shows to what extent the measurement and feedback control process drives informational active matter out of equilibrium. In order to assess what nonequilibrium states are reached and how they evolve, we focus on the steady-state limit ($t_m/\tau_{col} \ll 1$) and turn to a kinetic theory that includes the effects of active phase space compression.

Kinetic theory with compressible phase space

Within the framework of kinetic theory (77–79), we start with the Boltzmann equation,

$$\partial_t f + \boldsymbol{v}\cdot\nabla_{\boldsymbol{x}} f + \boldsymbol{F}\cdot\nabla_{\boldsymbol{v}} f = \mathcal{C}[f] \tag{4}$$

where $f(t, \boldsymbol{x}, \boldsymbol{v})$ is a single particle velocity distribution function, $\boldsymbol{F}$ represents external forces (that we neglect here), and $\mathcal{C}$ is the collision operator, which describes the manner in which particle collisions redistribute probability density in phase space. To account for the diameter feedback control process, we consider a modified version of the usual Boltzmann quadratic collision operator

$$\mathcal{C}[f] = \int (g_+ - g_-) d\sigma d\boldsymbol{v}_* \tag{5}$$

in which $g_+ = \alpha(\boldsymbol{v}, \boldsymbol{v}', \boldsymbol{v}_*, \boldsymbol{v}'_*) B(\sigma, \Delta\boldsymbol{v}) f(\boldsymbol{v}') f(\boldsymbol{v}'_*)/2$ and $g_- = B(\sigma, \Delta\boldsymbol{v})$
$f(\boldsymbol{v}) f(\boldsymbol{v}_*)/2$, where $\boldsymbol{v}$ and $\boldsymbol{v}_*$ are the velocities of particles undergoing collision, $\boldsymbol{v}'$ and $\boldsymbol{v}'_*$ are their postcollision velocities, and $\Delta\boldsymbol{v} = \boldsymbol{v} - \boldsymbol{v}_*$. The collision kernel $B = B(\sigma, \Delta\boldsymbol{v})$ describes the scattering of particles for a given impact parameter σ.

Crucially, the feedback-controlled bias of transitions between velocity states introduces distortions of phase space represented by an $\alpha(\boldsymbol{v}, \boldsymbol{v}', \boldsymbol{v}_*, \boldsymbol{v}'_*) \neq 1$ term. When detailed balance holds, $\alpha = 1$ and the steady-state solution of Eq. 4 is the MB distribution. This is not the case with the demon gas, where α is generically a function of measured microscopic properties of the system, eg velocities. Dissipation in granular media (80) or mechanical self-propulsion in flocking media (81) can also introduce such compressible phase space flows. In particular, the alignment rules in flocking can be interpreted as the result of information processing and decision making at the level of the agents (8, 82–86). In usual models of flocking like the Vicsek model, however, it is difficult to keep track of information exchanges and to disentangle the fully informational (entropic) part from the part requiring mechanical work.

For the demon gas, the collision operator should describe the evolution of a variable-diameter hard disk gas. Therefore, the collision kernel B takes on the form for hard disk collisions (see Materials and methods and SI Section S5), while α is a ratio of collision cross sections before and after the collision. For homogeneous demon gases, with diameter functions of velocity only, α can be shown to have the form (see Materials and methods)

$$\alpha = \frac{D(\boldsymbol{v}') + D(\boldsymbol{v}'_*)}{D(\boldsymbol{v}) + D(\boldsymbol{v}_*)}. \tag{6}$$

Only treating diameter as a function of single-particle velocities greatly simplifies the problem but requires other inputs to the diameter function (such as the average local velocity considered in the flocking example above) to be treated as constants. This amounts to requiring a separation of timescales, with single-particle velocities assumed to evolve much faster than the average of their local neighborhood. In the SI (Sections S5 and S6), we show that the steady-state distribution function can be written as $f^d = (1 + \mathcal{D}) f^{MB}$ as a function of the MB distribution f^{MB} and a function $\mathcal{D}(\boldsymbol{v})$ that preserves the conservation of particle number, linear momentum, and kinetic energy. The nonequilibrium distribution f^d allows entropy to be directly calculated in the small-density limit, and this quantity bounds how much work the excited demon gas state could perform on an external system as it relaxes to an equilibrium state (72).

Comparison between kinetic theory and simulation demonstrates strong agreement in the limit of small diameter changes and densities. Figure 3a–c compare a numerically simulated gas and properties derived from a seminumerically obtained velocity distribution function.

Kinetic theory further allows us to evaluate the rate of entropy production as (77, 78, 87)

$$\frac{dS}{dt} = \frac{k_B}{2} \int (g_+ - g_-) \ln \frac{g_+}{g_-} d\sigma\, d\boldsymbol{v}_*\, d\boldsymbol{v}, \tag{7}$$

from the Boltzmann equation, in which $g_\pm$ are the same as in Eq. 5. From this equation, which is reminiscent of the Schnakenberg formula for systems described by a master equation (88), it becomes apparent that the active compression of phase space (α in g_+) drives the system out of equilibrium. The resulting entropy production rate for several diameter functions are shown in Fig. 2k as a function of mean excess free energy (ie excess entropy) $\langle \mathcal{F} - \mathcal{F}^{MB} \rangle$. As shown in the figure, the entropy production rate is a monotonic function of excess entropy.

The velocity distribution for arbitrary diameter functions of velocity $D(\boldsymbol{v})$ can be obtained by a seminumerical method (see Materials and methods), as shown in Fig. 2f–j. The MB distribution (Fig. 2f) is deformed by nonconstant diameter functions producing lower-entropy distribution functions with broken symmetries (Fig. 2g–j). To obtain the nematic flocking state, we have used a diameter function that breaks isotropy (Fig. 2j). Breaking the 4-fold rotational symmetry of the gas is sufficient to obtain a finite $\boldsymbol{Q}$ in the steady state. If we instead break parity symmetry in the velocity plane ($\boldsymbol{v} \to -\boldsymbol{v}$, Fig. 2i), a heat flux $\boldsymbol{q} \neq 0$ entering the equation of conservation of energy can arise in the steady state. This can be predicted from the kinetic theory, which agrees well with numerical results obtained for small diameter changes (see Fig. 3c). In the presence of a linear momentum source or sink (ie another species of particle with different behavior), heat flux can be exploited to induce self-propulsion, as shown in Fig. 3d (see also SI Section S4). Departure from equilibrium values of distribution moments generically scales with ΔD, as shown in Fig. 3ei–gv.

Hydrodynamic theory of informational flocking

We now derive a hydrodynamic description of the flocking demon gas (with diameter function described in Fig. 1d–f) using a

Downloaded from academic.oup.com/pnasnexus/article/5/4/pgag077/8540115 by guest on 04 November 2026

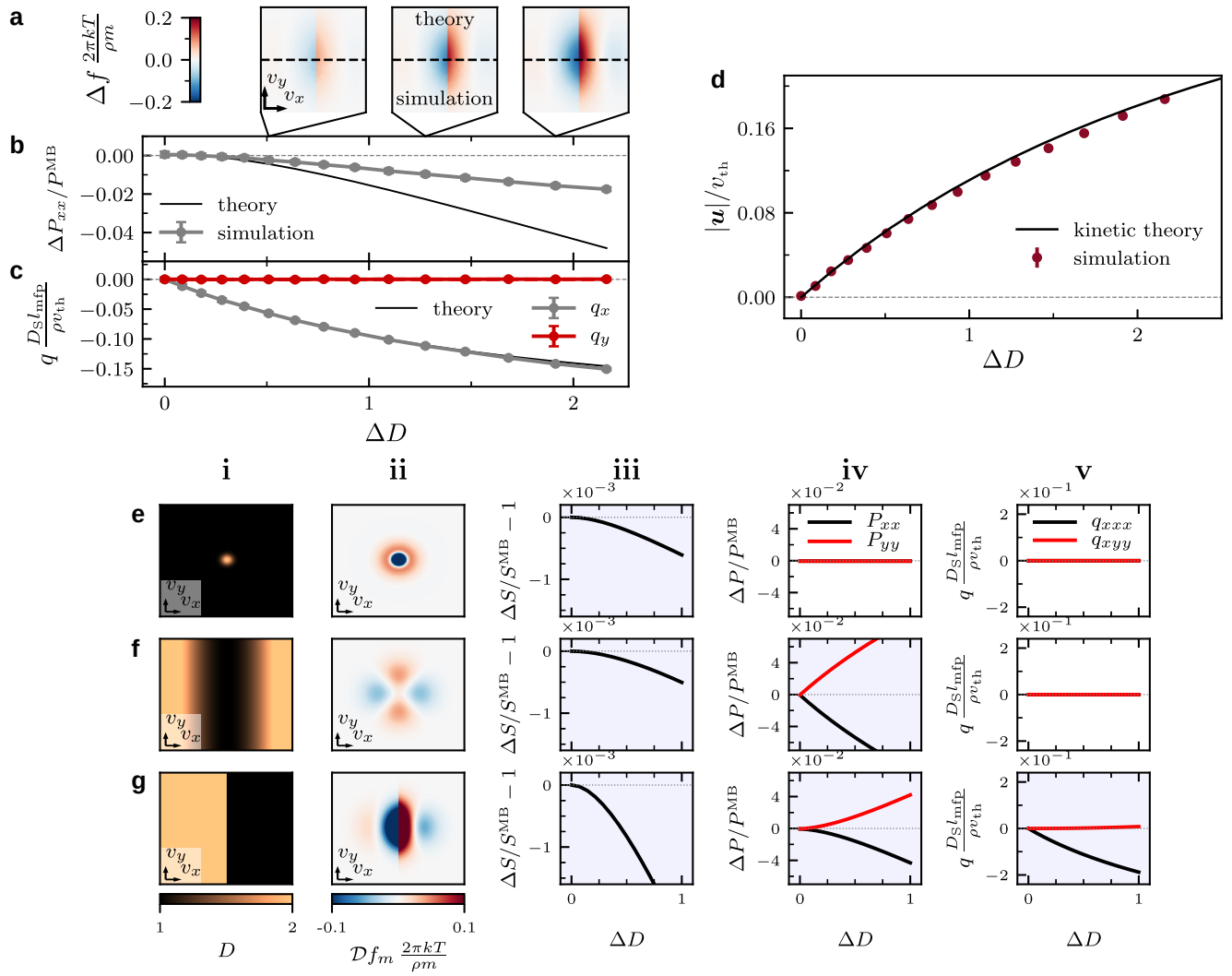

Figure 3 Observable consequences of demon gas measurements. a) Comparison of demon gas velocity distribution functions (relative to the MB distribution, $\Delta f = f^d - f^{\rm MB}$) obtained by kinetic theory (top) and by MD simulation (bottom) at various diameter differences for a diameter step function. b) Comparison of the pressure component (relative to MB, $\Delta P = P^d - P^{\rm MB}$) aligned with the step function normal (denoted x) from kinetic theory and MD simulation. c) Comparison of heat flux parallel and perpendicular to the step function normal. Heat flux is normalized by small diameter $D_{\rm S}$, mean free path $l_{\rm mfp}$, density ρ and thermal speed $v_{\rm th}$. d) Comparison of the average speed of demon particles immersed in an isothermal passive (fixed-diameter) gas, obtained by MD simulation and from kinetic theory. Heat flux generated by diameter change interacts with the passive species and results in net drift. (i) Diameter in the velocity plane, (ii) deviation from the MB distribution, (iii) distribution entropy ($S = \int f^d \ln f^d d\boldsymbol{v}$) relative to the MB distribution, (iv) pressure ($P_{ij} = \rho m \int v_i v_j f^d d\boldsymbol{v}$) relative to the MB distribution, and (v) heat flux ($q_i = (\rho m/2)\int v_i |\boldsymbol{v}|^2 f^d d\boldsymbol{v}$) for e) a radially symmetric Gaussian diameter function, f) an anisotropic quadratic function, and g) a step function.

single relaxation time approximation (89) adapted to the demon gas. In addition to the standard Navier–Stokes equations manifesting the conservation of mass, linear momentum, and energy (which are left unaffected), we find that the traceless part $Q_{ij} = P_{ij} - (P_{kk}/2)\delta_{ij}$ of the pressure tensor P_{ij} evolves as

$$\frac{DQ_{ij}}{Dt} = \partial_k R_{ijk} + \frac{1}{\tau}\left[\frac{Q_0}{Q} - 1\right]Q_{ij} \tag{8}$$

in which τ is a relaxation time, $Q^2 \equiv \|\boldsymbol{Q}\|^2 \equiv Q_{\mu\nu}Q_{\nu\mu}/2 \geq 0$, D/Dt is the material derivative, and

$$Q_0 = \frac{4P_0}{\pi}\frac{\Delta D}{\Delta D + 2D_S}, \tag{9}$$

where $P_0 = \rho k_B T$ and R_{ijk} is a higher-order current (see SI Section S7 for details).

In the homogeneous case, Eq. 8 implies that the order parameter Q quantifying the nematic flocking evolves as

$$\partial_t Q = \frac{1}{\tau}[Q_0 - Q] \tag{10}$$

while the direction of the principal axes of the symmetric tensor $\boldsymbol{Q}$ (corresponding to the nematic flocking direction) stays fixed.[b] In the language of dynamical system theory, this describes a non-analytic version (90) of a circle-pitchfork bifurcation (91) occurring at $Q_0 = 0$. When $Q_0 > 0$, there is a circle of stable solutions $\boldsymbol{Q}$ with $Q = Q_0$ and an arbitrary orientation ψ.[c]

The steady-state solution of Eq. 10 is shown in Fig. 2l and compared with numerical data. The data collected for a gas with fixed anisotropy axis (explicitly broken symmetry, blue data) is nearly linear in Q_0, as predicted (note that $\langle|Q|\rangle$ does not approach 0 as $Q_0 \to 0$ due to thermal fluctuations).

Downloaded from academic.oup.com/pnasnexus/article/5/4/pgag077/8540115 by guest on 04 November 2026

The anisotropy of the gas is a weak function of temperature, remaining nearly constant as temperature is increased 50-fold (Fig. 2m). Theory predicts that Q/P_{kk} has no temperature dependence, thus observed trends in the simulations indicate a higher-order correction. Simple arguments based on coupling between nearby regions in the spatially extended gas, corresponding to adding diffusive terms in Eq. 8 by linear response (eg $R_{\mu\nu\rho} \propto \partial_\rho Q_{\mu\nu}$), predict alignment of ψ in the absence of fluctuations.

Measurement-induced flocking transition

Going back to information thermodynamics, the steady-state magnitude of the order parameter $\boldsymbol{Q}$ (ie Q_0) is bounded by the quantity of information measured. Indeed, the work $W(Q_0)$ that the gas can exert on another system during relaxation to the MB distribution is bounded by $\Delta\mathcal{F}^*$ (72), which in turn is bounded by $k_B T I$. For the case of the flocking diameter function and to lowest order in activity (ΔD), we find that $\Delta\mathcal{F}^* = \frac{1}{2} k_B T (\frac{\pi Q_0}{4P_0})^2$. Hence, we get

$$\left(\frac{Q_0}{P_0}\right)^2 \leq \frac{32}{\pi^2} I. \tag{11}$$

In other words, the magnitude Q_0 of the informational flocking order parameter is bounded by the information I accumulated through continuous measurements. This suggests viewing the transition to informational flocking as a classical measurement-induced phase transition (57–61).

In quantum MIPTs (62–64), local projective measurements may counteract the scrambling of information originating from the underlying unitary dynamics. Here, the combination of local measurements and control actions may counteract the scrambling of information originating from the underlying chaotic dynamics (eg collisions in the gas). Classically, the act of measurement itself does not affect the system[d] so, as in Refs. (59–61), control actions are performed that modify the state of the system according to the outcome of the measurements. In contrast with these works, here microscopic control actions are not necessarily designed to mimic quantum measurements, but include bioinspired behavioral decisions.

Exploiting nonthermal noise

At scales beyond several μm, thermal noise will be too weak to agitate information-processing agents, while nonthermal noise sources (turbulence, vibration) are common. Here, we use a pattern formation task to demonstrate that nonthermal noise can be used to produce low-entropy collective macrostates even in complex fluctuating environments. We consider two populations of particles (blue and red) that tend to move in opposite directions $\pm\boldsymbol{\xi}(\boldsymbol{x})$ set by a fixed field $\boldsymbol{\xi}(\boldsymbol{x})$. The linear momentum conservation of our model does not preclude the formation of density patterns in single-species gases with diameter functions of position; Fig. 4 demonstrates the formation of a density gradient for a demon gas with a choice function which depends on particle location and velocity. However, momentum exchange between two species greatly enhances informational-self propulsion.

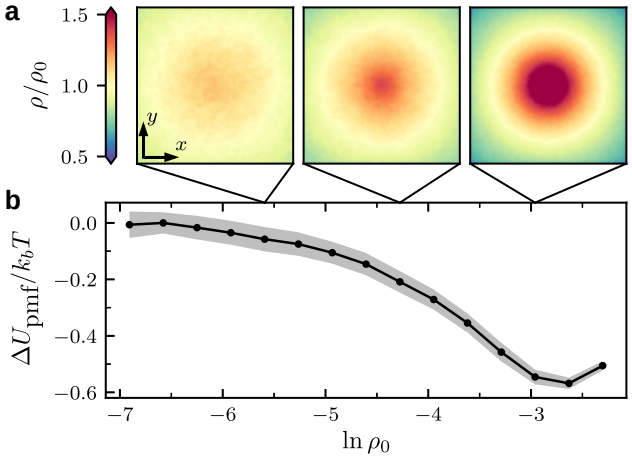

Figure 4 Nonuniform density of a pure demon gas. a) Snapshots of a demon gas with diameter function $D = D_S + \Delta D\mathcal{H}(-\boldsymbol{v}\cdot\boldsymbol{x})$. Increasing initial density ρ_0 leads to a greater density enhancement near $\boldsymbol{x} = 0$. b) The maximum depth of the potential of mean force as initial density ρ_0 is increased. Until $\ln\rho_0 \approx -2.4$ increasing density enhances the depth of the potential well. At greater densities, crowding effects begin to inhibit demon particle size changes.

Using reinforcement learning (RL) techniques from the field of policy optimization (92) (Fig. 5a), we find that demon gas propulsion is maximized for diameter functions of the form

$$D(\boldsymbol{v}, \boldsymbol{x}) = D_S + \Delta D\mathcal{H}\big(-\boldsymbol{v}\cdot\boldsymbol{\xi}(\boldsymbol{x})\big), \tag{12}$$

where $\boldsymbol{\xi}$ is a vector field pointing along the direction of transport (Fig. 5b–h). Regardless of noise ensemble (thermalized, mimicking a granular vibration table, or even a bath of self-propelled active particles) Eq. 12 is effective at producing robust flows.

Figure 6a and SI video V1 show the dynamics of two populations of informational particles dropped onto a surface. Elastic collision of particles with the surface and each other in the presence of linear drag produces a nonthermal and nonstationary noise that the information-processing particles harness to create an S-shaped pattern. Energy is dissipated via linear drag, eventually resulting in a stationary state. This process can also be sustained for constantly agitated systems, see SI video V2. Note that species separation can be observed in systems as small as $N = 125$ particles (Fig. 7).

In Fig. 6b, c, we compare patterns formed by continuously agitated variable-diameter demon particles and fixed-diameter particles with the ability to self-propel. In both cases, particles are aware of $\boldsymbol{\xi}$, however in the case of propelled particles it is used to set the propulsion direction, equivalent to an externally applied potential $\nabla U(\boldsymbol{x}) = -f_w\boldsymbol{\xi}$. The magnitude of their propulsive force, f_w, controls how far this system departs from equilibrium, whereas ΔD plays an analogous role for demon particles. Self-propelled particles demix (Fig. 6b) into the desired pattern. However as nonthermal agitation is increased, the patterns become less and less visible because of the noise (expressible as an effective temperature $T_{\rm eff}$). In contrast, the resolution of patterns formed by demon particles experiencing the same agitation (and following $\boldsymbol{\xi}$) appears to improve with additional noise (Fig. 6c). In fact, the infinite-time resolution of demon particles is entirely independent of the level of noise, while the time required to obtain a given resolution decreases with effective temperature, $\propto 1/\sqrt{T_{\rm eff}}$.

Downloaded from academic.oup.com/pnasnexus/article/5/4/pgag077/8540115 by guest on 04 November 2026

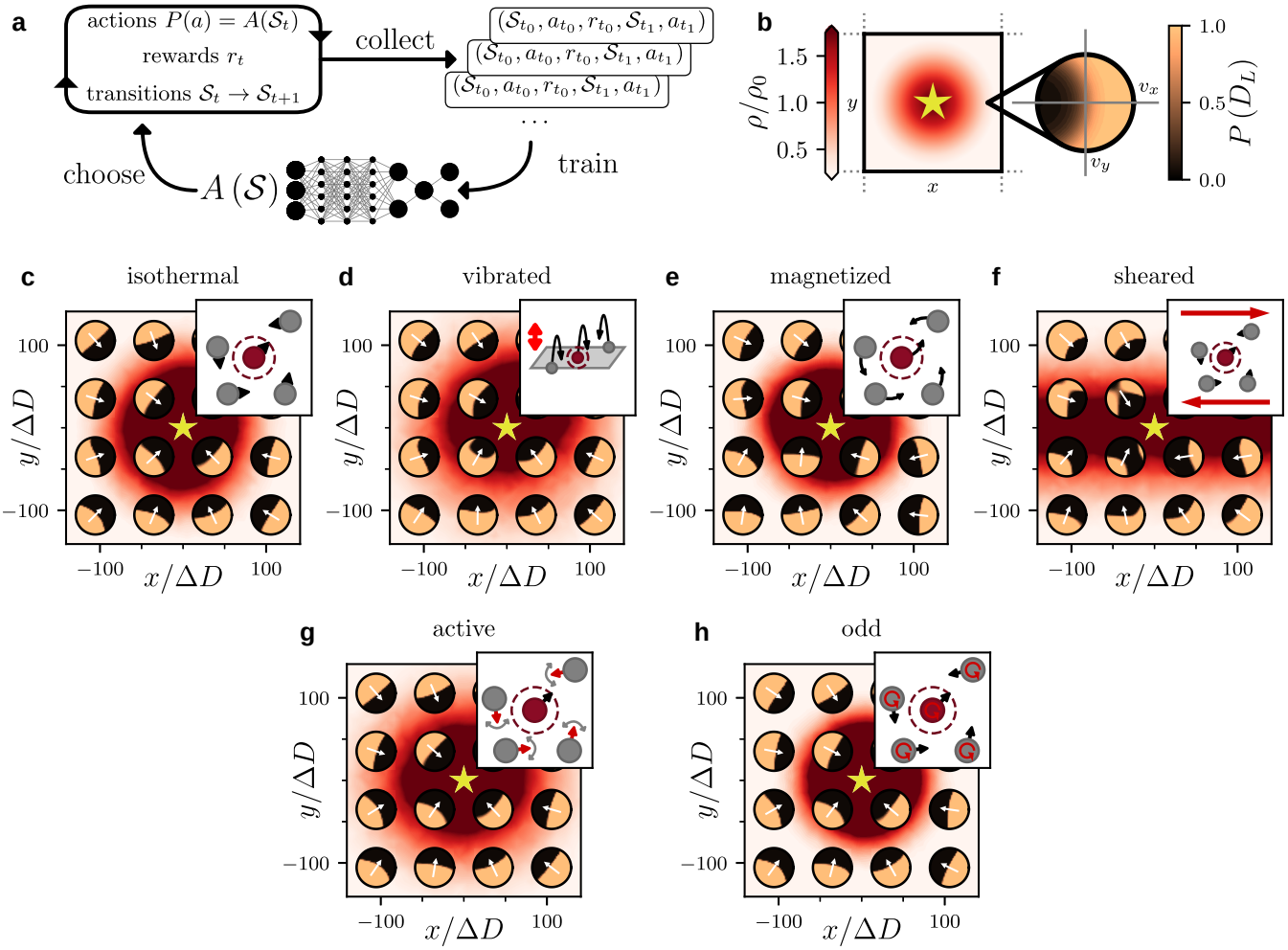

Figure 5 Biasing strategies for demon particles via reinforcement learning (RL). a) The RL learning cycle. Actions are chosen according to a policy function, and experiences of transitions are accumulated in a buffer. This buffer is used to train a feed-forward artificial neural network that defines the policy function. b) Locomotion task definition and legend. Agents are embedded in a periodic environment with a singly peaked (indicated by star) reward function. Agent density after learning is shown as a heat map. The RL algorithm searches for a probabilistic discrete diameter function of $\boldsymbol{v}$, $\boldsymbol{x}$ that most rapidly moves agents toward the maximum. Plots in (c–f) follow the same color scheme as (b). c–h) RL diameter functions under various transport physics. Microscopic particle motions (arrows) are schematically represented in insets. In all cases, the vector field found by odd moments over the learned diameter distribution ($\boldsymbol{\xi}$) points along the shortest-time path toward the reward maximum (main panel arrows). c) Isothermal environment. d) Vibrated granular bed environment. e) Isothermal dynamics with applied magnetic field. f) Langevin dynamics with applied shear field. g) Active gas bath. Active particles have a fixed-magnitude force pointing along their rotationally diffusing director. h) Odd gas bath, in which all particles experience an equal and opposite transverse force during collisions, in addition to the usual hard core repulsion. See SI Section S1 for various simulation details and parameters.

The finite-time resolution is set by propulsion speed. Returning to a thermal system in which a demon gas is immersed in a fixed-diameter isothermal gas, kinetic theory (Fig. 6d-e) accurately predicts that the mean flow of the informational gas takes the form

$$u_i = -\frac{m}{2k_bT}\int v_i|\boldsymbol{v}|^2 f^d d\boldsymbol{v} = a(\rho, \Delta D)\sqrt{2k_bT/m}. \tag{13}$$

The demon gas effectively converts a temperature-independent fraction ($a(\rho, \Delta D)$) of the mean thermal kinetic energy into directed motion.

The noise-independence of patterns at long times arises due to the balancing of two effects which scale identically with noise. Returning again to a thermal system of demon gas particles, but now considering a diameter function of both velocity and location (Fig. 6f), we observe density gradients resulting from particle measurements. An empirical effective potential, the so-called potential of mean force, $U_{\text{pmf}}(\boldsymbol{x}) = -k_bT \ln \rho(\boldsymbol{x})/\rho_0$, can be computed to compare the system to one bound by an energetic potential (93). In Fig. 6g, the effective potential depth (ΔU_{pmf}) is found to scale linearly with temperature, entirely compensating the effect of noise.

Similar effects occur in the nonthermal environment of Fig. 6c, and consequently increasing k_bT_{eff} improves the short-time resolution of pattern-forming demon gas particles, while having no effect on their eventual steady state. Meanwhile, pattern formation under a temperature-independent driving force (eg self-propulsion as in Fig. 6b) only degrades with additional noise.

Conclusion

Our results shed light on collective processes which exploit measurement and noise to produce nonequilibrium steady

Downloaded from academic.oup.com/pnasnexus/article/5/4/pgag077/8540115 by guest on 04 November 2026

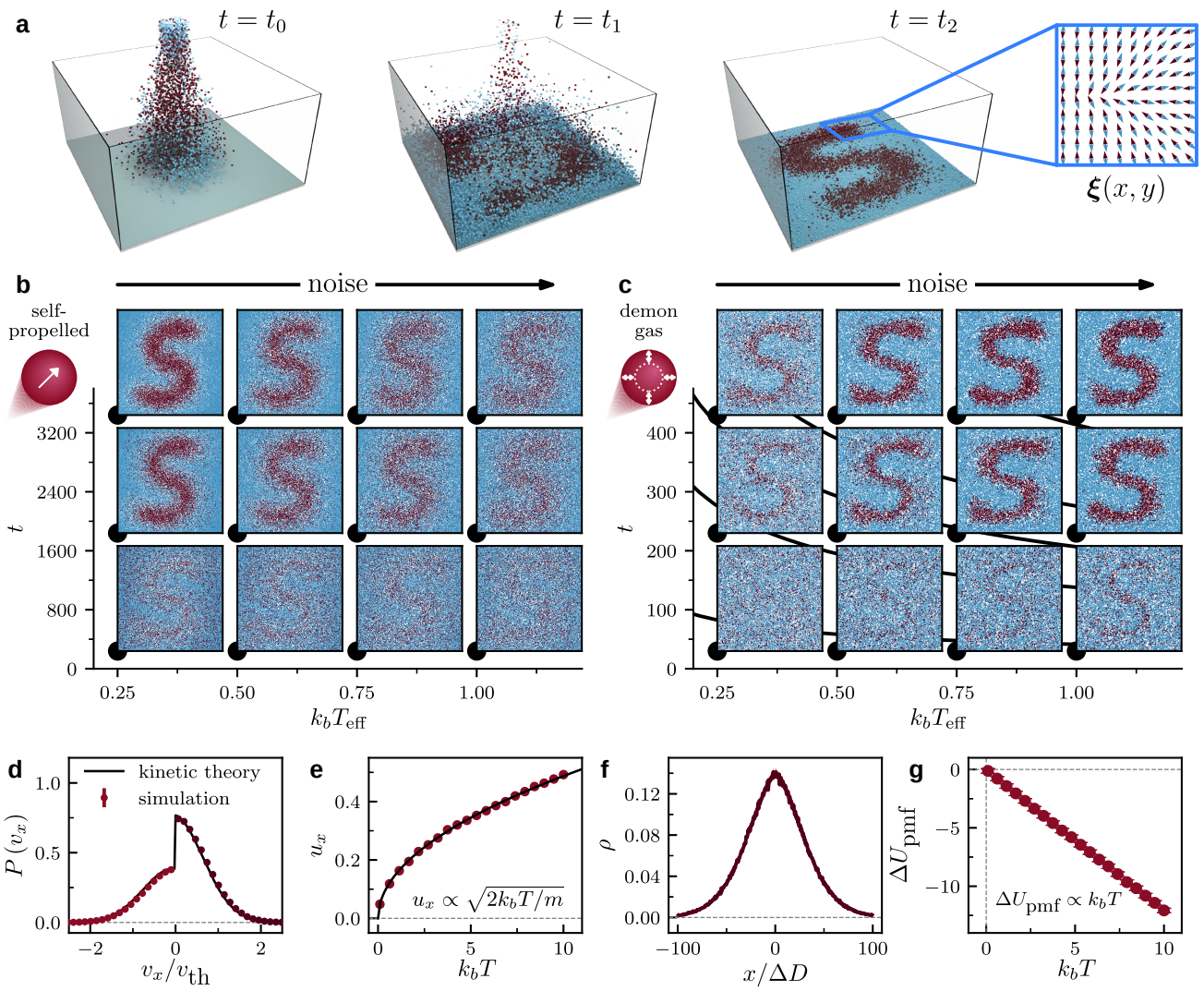

Figure 6 Noise-driven active patterning. a) A collection of variable-diameter particles are dropped into a hard-sided box. As particles undergo elastic collisions, their velocities are reduced by a linear drag ($\gamma = 0.01$) term and they settle onto the bottom of the box. The two species (dark and light) have opposite $\boldsymbol{\xi}(\boldsymbol{x})$ fields (inset), driving separation into a designed pattern. b) Self-propelled particles that exert a constant magnitude force in the direction specified by $\boldsymbol{\xi}$ (ie light (dark) particles push themselves away from (toward) the nearest segment of the pattern), while experiencing constant agitation (linear drag $\gamma = 0.01$, random forces with mean magnitude $6k_bT_{\text{eff}}\gamma/\delta t$, see Materials and methods for details). As agitation is increased (k_bT_{eff}), pattern resolution degrades, since particles can only push with a fixed amount of force. Frames are instantaneous snapshots of simulations at the time and effective temperature indicated by the position of the inset lower left corner. c) Demon gas particles following the diameter rule of Eq. 12 and the same $\boldsymbol{\xi}$ field and nonthermal agitation as (b). The time required to obtain a given resolution decreases with increasing agitation. Black curves are $t = sL/\langle|\boldsymbol{v}|\rangle$ for $s = 0.15 \rightarrow 2$, where L is the size of the simulation domain and $\langle|\boldsymbol{v}|\rangle = \sqrt{2k_bT_{\text{eff}}/m}$ is the mean speed of a particle in the gas. d) Velocity distribution function of demon gas particles that adopt small (large) diameters when traveling right (left) immersed in a fixed-diameter isothermal gas. Exchange of linear momentum with the passive gas allows the demon gas to concentrate in the positive half of the velocity plane, as predicted by kinetic theory. e) Mean bulk velocity u_x of the demon gas in (d) as a function of temperature, with fixed $\Delta D = 1$. Mean bulk flow due to collisional biasing is a fraction of the thermal speed. f) Density of demon gas particles that adopt small (large) diameters when moving toward (away) from the origin. Selective collisions with each other and a surrounding passive isothermal gas concentrate them near the target location. g) Depth of an effective potential consistent with the increased density of demon gas particles near the target in (f), as a function of temperature.

states in many-ratchet systems. Such processes are an important component of realistic systems where information processing and mechanical activity (eg self-propulsion) coexist. Both types of activity are engines (ie intermediaries between a nonequilibrated reservoir and a sink that generates work), however informational engines use their reservoir (ie memory, prepared by dissipative erasure) to selectively couple to the momentarily "hot" fluctuating environmental degrees of freedom. The conversion of noise into motive power requires control actions informed by measurements. In practice, these feedback mechanisms will always convert energy stored in some fuel, thus blurring the theoretical distinction between informational and mechanical activity. However at a fundamental level, measurements and the control actions they inform can be performed with arbitrarily small energy expenditure (zero, in the frictionless limit) as in the celebrated Feynman–Smoluchowski single-ratchet example (94). The only energy cost that is strictly required is the $k_BT\log 2$ per bit associated with erasing the memory registry, as stipulated by Landauer's erasure principle (66).

Saturating Landauer's bound may be difficult in practice, however a key aspect of informational driving is that work output scales with the magnitude of environmental fluctuations, which

Downloaded from academic.oup.com/pnasnexus/article/5/4/pgag077/8540115 by guest on 04 November 2026

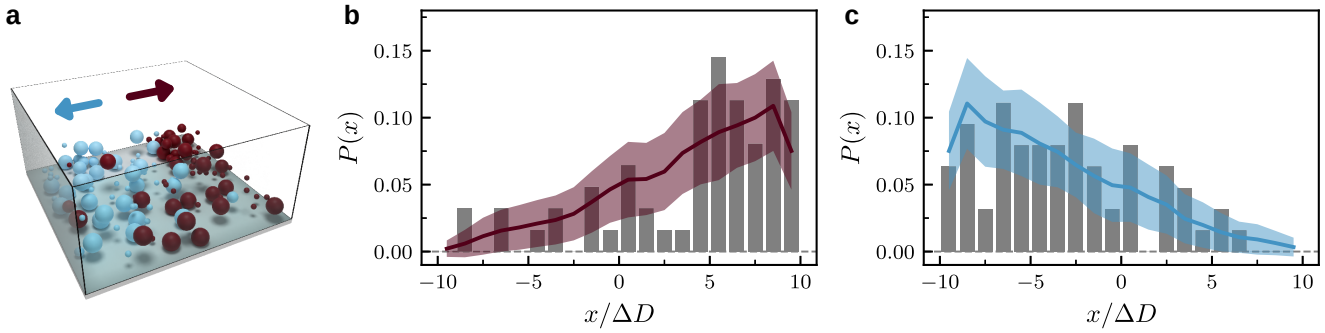

Figure 7 Separation in a small vibrated demon system. a) A small system of demon particles ($N = 125$) agitated by vertical forces and confined within a smooth-sided container. Dark (light) particles attempt to move to positive (negative) x positions. b) Probability of finding dark particles at a given x location within the container. Bars are data from one instant (as pictured in a), data is the mean and one standard deviation calculated from 250 subsequent snapshots. c) Data equivalent to b for light particles. Species separation is apparent even in a single snapshot. See SI Section S1 for simulation details and parameters.

we show can be exploited even for nonthermal reservoirs in which fluctuations can be very large. Hence, the practical difference between these two flavors of nonequilibrium driving resembles the distinction between electrical rectifiers and batteries. Informational driving, like a rectifier, produces bias from a fluctuating bias-free input, while a battery (like conventional self-propulsion) directly converts a chemical fuel into a bias.

The core concepts of informational activity investigated here by kinetic theory in classical many-ratchet thermal systems and extended to nonthermal systems with reinforcement learning, may also apply to animal, bacterial, and micro-robotic swarms that collectively seek to harness environmental noise to power goal-directed behaviors, and in which measurement-induced phase transitions similar to the measurement-induced flocking described in this work may also occur. This perspective may also be fruitful in the context of recently proposed active quantum systems (95–98).

Materials and methods

Numerical model implementation

MD simulations of the demon gas were performed with the open-source software package `HOOMD-Blue` (v2.9.3) (99). All particles interact through a shifted Weeks–Chandler–Andersen potential (100), where the origin is shifted so that the radius of the particle is the potential's zero isoenergy surface. This surface was modified by a custom updater in accordance with a diameter function. Depending on the simulation, particles were simulated with velocity Verlet integration and a Nosé–Hoover thermostat or Langevin thermostat, as implemented in `HOOMD-blue`. See SI Section S1 for details of each type of simulation employed.

Free energy impulse fitting model

In Fig. 2b–e, the free energy change of a demon gas after measurement is fit to a simple functional form to extract estimates of the amount of free energy injected per measurement event. Here, we outline the fitting procedure. The free energy is computed from the (Shannon) entropy of a numerically sampled velocity distribution function. (See SI Section S1 for numerical simulation details.) We subtract off the MB entropy as a baseline, and model the effect of measurement as a unidirectional coupling between the information-carrying degree of freedom (the diameters), and the velocity degrees of freedom. We assume that the free energy of the information carrying degree of freedom ($\mathcal{F}_{\text{ic}}$) receives impulses of strength $\mathcal{F}_m$ due to measurement which add to any elevated free energy remaining from the previous measurement ($\Delta\mathcal{F}^*$), and relaxes exponentially with a single timescale τ,

$$\frac{d}{dt}\mathcal{F}_{\text{ic}} = -\frac{1}{\tau}\mathcal{F}_{\text{ic}} \tag{14}$$

$$\mathcal{F}_{\text{ic}} = (\mathcal{F}_m + \Delta\mathcal{F}^*)e^{-\frac{t}{\tau}}, \tag{15}$$

where we take $t = 0$ as the time of measurement. Relaxation of $\mathcal{F}_{\text{ic}}$ is assumed to occur by coupling to the velocity degrees of freedom ($\mathcal{F}$). The velocity degrees of freedom are also assumed to exponentially relax to equilibrium (with the same timescale τ),

$$\frac{d}{dt}\mathcal{F} = -\frac{d}{dt}\mathcal{F}_{\text{ic}} - \frac{1}{\tau}\mathcal{F} \tag{16}$$

$$\mathcal{F} = \left(\Delta\mathcal{F}^* + (\mathcal{F}_m + \Delta\mathcal{F}^*)\frac{t}{\tau}\right)e^{-\frac{t}{\tau}} \tag{17}$$

To fit these parameters, several simulated measurement intervals t_m were observed and the resulting free energy curves are collapsed onto the range $[0, t_m]$. The parameters $\mathcal{F}_m$, $\Delta\mathcal{F}^*$, and τ can be seen in SI Fig. S1 a, b, and raw free energy curves along with their fit lines can be seen in SI Fig. S1 d–l. Bootstrap fitting error is shown in SI Fig. S1 a–c.

Kinetic theory of variable diameter hard disks

Conservation of momentum and energy determine the velocities of a pair of hard disks after collision. Assuming uniform particle masses,

$$\boldsymbol{v} + \boldsymbol{v}_* = \boldsymbol{v}' + \boldsymbol{v}'_* \tag{18}$$

$$|\boldsymbol{v}|^2 + |\boldsymbol{v}_*|^2 = |\boldsymbol{v}'|^2 + |\boldsymbol{v}'_*|^2. \tag{19}$$

Downloaded from academic.oup.com/pnasnexus/article/5/4/pgag077/8540115 by guest on 04 November 2026

If $\hat{n}$ is a unit vector that points between disk centers at the point of contact (note that $\hat{n}$ therefore depends upon diameter), then the postcollision velocities can be written,

$$\boldsymbol{v}' = \boldsymbol{v} - ((\boldsymbol{v} - \boldsymbol{v}_*) \cdot \hat{n})\hat{n} \tag{20}$$

$$\boldsymbol{v}'_* = \boldsymbol{v}_* + ((\boldsymbol{v} - \boldsymbol{v}_*) \cdot \hat{n})\hat{n}. \tag{21}$$

For disks of fixed diameter, this scattering process is microreversible; $(\boldsymbol{v}, \boldsymbol{v}_*)$ maps to $(\boldsymbol{v}', \boldsymbol{v}'_*)$ and $(-\boldsymbol{v}', -\boldsymbol{v}'_*)$ maps to $(-\boldsymbol{v}, -\boldsymbol{v}_*)$, resulting in a Jacobian for the change of variables equal to -1 (77). This one-to-one mapping allows all four velocity terms to be collected under a common unit disk integration in the typical quadratic Boltzmann collision operator (see SI Section S5 for additional details). When particle diameters are instead functions of velocity, the microreversibility of the collision process is broken but can be restored with a shift of relative positions. In a coordinate frame centered on the point of contact for the forward collision, a shift in position of $\alpha = (D(\boldsymbol{v}') + D(\boldsymbol{v}'_*))/(D(\boldsymbol{v}) + D(\boldsymbol{v}_*))$ along the reflection plane of the forward collision, applied to one particle during the reverse process restores the symmetry of velocity mapping (see SI Fig. S5). Note that when demon gas particles are immersed in a fixed-diameter gas, one set of diameters (starred or unstarred) is constant.

We now solve for the single particle probability distribution function ($f(\boldsymbol{v})$) that satisfies the steady state form of Eq. 4 for the demon gas collision operator by examining the collision invariants of the gas. If we consider a moment of the time-varying distribution function $f(\boldsymbol{v}, t)$ with a nontime-varying test function ϕ:

$$\langle \phi \rangle_f = \int f(\boldsymbol{v}, t)\phi(\boldsymbol{v})d\boldsymbol{v}, \tag{22}$$

the time evolution of this quantity is

$$\frac{d}{dt}\langle \phi \rangle_f = \int \phi(\boldsymbol{v})\mathcal{C}(f)(\boldsymbol{v}, t)d\boldsymbol{v}. \tag{23}$$

The function ϕ can be brought into the integrand of the collision operator since it is not a function of time. As we are now considering an expression integrating over all $\boldsymbol{v}$ and $\boldsymbol{v}_*$ (and by extension $\boldsymbol{v}'$ and $\boldsymbol{v}'_*$), the choice of primed and starred variables is entirely arbitrary. A typical procedure is to average over the exchange of velocity variables (77), producing the following for the case of $\alpha = 1$,

$$\frac{1}{8}\iiint(\phi + \phi_* - \phi' - \phi'_*)\left(f'f'_* - ff_*\right)B(\sigma, \Delta\boldsymbol{v})d\boldsymbol{v}_*d\boldsymbol{v}d\sigma, \tag{24}$$

where B is the collision kernel (see SI Section S5) and σ the impact parameter. If ϕ is a quantity that is conserved through the collision, then it remains unchanged and $\frac{d}{dt}\langle \phi \rangle_f = 0$. This defines a summational collisional invariant for the system. For the Boltzmann equation, summational invariants can only be linear combinations of the microscopically conserved quantities, $\mathcal{M} = 1, \boldsymbol{v}, |\boldsymbol{v}|^2$, which are unchanged during collision by construction (101). Therefore, there exist constants $(a, \boldsymbol{b}, c)$ that define any summational collision invariant:

$$h(\boldsymbol{v}) = a + \boldsymbol{b} \cdot \boldsymbol{v} + c|\boldsymbol{v}|^2. \tag{25}$$

For the demon gas with $\alpha \neq 1$, the same procedure of exchanging velocity variables allows a common term to be collected, $h = (D_{\text{const}} + D(\boldsymbol{v}))\phi$ for the mixed demon-passive case, or $h = D(\boldsymbol{v})\phi$ more generally. This term must satisfy the same condition $h_* - h' - h'_* = 0$ for it to remain unchanged by collisions (ie be an invariant). Beginning with the MB velocity distribution function in 2D,

$$f^{\text{MB}}(\boldsymbol{v}) = \frac{m\rho}{2\pi kT}e^{-\frac{m|\boldsymbol{p}|^2}{2kT}}, \tag{26}$$

where $\boldsymbol{p} = \boldsymbol{v} - \langle \boldsymbol{v} \rangle = \boldsymbol{v} - \boldsymbol{u}$ is the velocity of the gas in the flow frame, we express the demon gas distribution function as $f^d = (1 + \mathcal{D})f^{\text{MB}}$, where $\mathcal{D}$ is a function of velocity only. We can treat the function $(1 + \mathcal{D})$ as a test function operating on the MB distribution, with collisional invariant $h = D(1 + \mathcal{D})$. The four constants a, b_x, b_y, c which define invariant h (and therefore $\mathcal{D}$) can be found by requiring that the first four conserved moments ($\mathcal{M}$) of the demon gas velocity distribution are equal to the first four moments of the equilibrium MB distribution,

$$\begin{aligned} \int \mathcal{M}f^{\text{MB}}d\boldsymbol{v} &= \int \mathcal{M}(1 + \mathcal{D})f^{\text{MB}}d\boldsymbol{v} \\ 0 &= \int \mathcal{M}\mathcal{D}f^{\text{MB}}d\boldsymbol{v}, \end{aligned} \tag{27}$$

ie the demon gas conserves number, momentum, and energy in all collisions. Note that this restriction does not constrain the third-order moments which define the heat flux tensor, or the individual entries of the pressure tensor (derived from second-order moments).

From the expression for the demon gas collision invariant, one obtains $(1 + \mathcal{D}) = hD^{-1}$. Note that if $D = 0$ in some region around a point $\boldsymbol{v}_0$, then this region would become a sink for gas density and the entire gas would eventually come to reside there without further collisions. Expressing the expectation value over f^{MB} as $\langle \phi \rangle_m = \int \phi f^{\text{MB}}d\boldsymbol{v}$,

$$\begin{aligned} \langle \mathcal{M} \rangle_m &= \langle \mathcal{M}(1 + \mathcal{D}) \rangle_m \\ &= \langle \mathcal{M}hD^{-1} \rangle_m \\ &= a\langle \mathcal{M}D^{-1} \rangle_m + b_x\langle \mathcal{M}v_xD^{-1} \rangle_m \\ &\quad + b_y\langle \mathcal{M}v_yD^{-1} \rangle_m + c\langle \mathcal{M}|\boldsymbol{v}|^2D^{-1} \rangle_m. \end{aligned} \tag{28}$$

For each of the conserved moments ($\mathcal{M} = 1, v_x, v_y, |\boldsymbol{v}|^2$) a new expression is generated, allowing for the definition of a full rank system of linear equations,

$$\mathcal{A} \cdot G = \mathcal{B} \tag{29}$$

$$\mathcal{A} = \begin{bmatrix} \langle \frac{1}{D} \rangle_m & \langle \frac{v_x}{D} \rangle_m & \langle \frac{v_y}{D} \rangle_m & \langle \frac{|\boldsymbol{v}|^2}{D} \rangle_m \\ \cdot & \langle \frac{v_x^2}{D} \rangle_m & \langle \frac{v_xv_y}{D} \rangle_m & \langle \frac{v_x|\boldsymbol{v}|^2}{D} \rangle_m \\ \cdot & \cdot & \langle \frac{v_y^2}{D} \rangle_m & \langle \frac{v_y|\boldsymbol{v}|^2}{D} \rangle_m \\ \cdot & \cdot & \cdot & \langle \frac{|\boldsymbol{v}|^4}{D} \rangle_m \end{bmatrix} \tag{30}$$

$$G = \begin{bmatrix} a & b_x & b_y & c \end{bmatrix}^{\top} \tag{31}$$

$$\mathcal{B} = \begin{bmatrix} \rho & \rho u_x & \rho u_y & \rho|\boldsymbol{u}|^2/2 + \rho kT \end{bmatrix}^{\top}, \tag{32}$$

where the matrix $\mathcal{A}$ is symmetric and redundant entries are not shown. Using the solution of this system of equations the demon gas velocity distribution can be written as

$$f^d = f^{\text{MB}}(1 + \mathcal{D}) = f^{\text{MB}}D^{-1}h = f^{\text{MB}}D^{-1}\left(\boldsymbol{M} \cdot (\mathcal{A}^{-1}\mathcal{B})\right), \tag{33}$$

where $\boldsymbol{M} = [1, v_x, v_y, |\boldsymbol{v}|^2]$. For arbitrary diameter functions, the terms in the matrix $\mathcal{A}$ and its inverse are most easily found by

Downloaded from academic.oup.com/pnasnexus/article/5/4/pgag077/8540115 by guest on 04 November 2026

numerical methods. See the Supplementary information for functional forms of $\mathcal{A}$ matrices for selected diameter functions.

Reinforcement learning for nonthermal environments

To explore the behavior of the demon gas model subjected to nonthermal noise sources, we implemented an extension in which the diameter function was represented by a feed-forward neural network. Using standard policy optimization algorithms (92, 102) (shown schematically in Fig. 5a and detailed in SI Section S1), the diameter function was optimized to bring particles to and keep them near the origin of mixed demon-passive simulations. Successful learning produced probabilistic diameter functions that drove demon particles to accumulate at high density near their goal (Fig. 5b). Figure 5c–h shows the result of learning across a variety of simulation types (detailed in the SI). In all cases, the dominant contribution to the diameter function took the form of Eq. 12, with $\boldsymbol{\xi}(\boldsymbol{x})$ pointing along the direction of least-time approach to the target location (white arrows).

Spontaneous symmetry breaking

To obtain a closed equation for the growth of local pressure asymmetry, the linear, single relaxation time collision operator approximation is used,

$$\mathcal{C}_{\text{lin}} = \frac{1}{\tau}\left(f^d - f\right), \tag{34}$$

where f^d is the steady-state demon gas velocity distribution and τ is the collision timescale. The time evolution of the mean of any function of velocity can therefore be estimated as Eq. 22, which produces equations of the form $d\langle\phi\rangle/dt = (\bar{\phi} - \langle\phi\rangle)/\tau$, where $\bar{\phi}$ is the mean value of the moment over the reference distribution f_d. For the diameter function described in Fig. 1d–f, f_d can also be found analytically,

$$f^d = \frac{a}{D(\theta)} f^{\text{MB}}, \tag{35}$$

where f^{MB} is the Maxwellian distribution and $a = 2D_S(D_S + \Delta D)/(2D_S + \Delta D)$. See SI Section S6 for details of this derivation and SI Section S7 for derivation of the hydrodynamic relations for $\boldsymbol{Q}$.

Notes

[a]The steady-state evolution over one period $0 \le t \le t_m$ is then $\mathcal{F}_{\text{ic}}(t) = \mathcal{F}_{\text{ic}}^{\text{MB}} + (\mathcal{F}_m + \Delta\mathcal{F}^*)e^{-t/\tau}$ and $\mathcal{F}(t) = \mathcal{F}^{\text{MB}} + (\Delta\mathcal{F}^* + (\mathcal{F}_m + \Delta\mathcal{F}^*)t/\tau)e^{-t/\tau}$. Imposing that $\mathcal{F}(0^-) = \mathcal{F}^{\text{MB}} + \Delta\mathcal{F}^*$ equals $\mathcal{F}(t_m^-) = \mathcal{F}^{\text{MB}} + (\mathcal{F}_m + \Delta\mathcal{F}^*)e^{-t_m/\tau}$ yields $\Delta\mathcal{F}^* = \mathcal{F}_m/T^*$, where $T^* = (e^{t_m/\tau} - 1)\tau/t_m - 1$. Combining expressions, the average value over a period is $\langle\mathcal{F}\rangle_{0\to t_m} = \mathcal{F}_m(2/T^* + 1)(-e^{-t_m/\tau}(t_m + \tau) + \tau)/t_m + \mathcal{F}^{\text{MB}}$.

[b]In the homogeneous case, Eq. 8 becomes $\partial_t Q_{ij} = [Q_0/Q - 1]Q_{ij}/\tau$. As $\boldsymbol{Q}$ is symmetric and traceless, it can be written as $\boldsymbol{Q} = x\boldsymbol{\sigma}_1 + y\boldsymbol{\sigma}_3$ in which $\boldsymbol{\sigma}_a$ are Pauli matrices. Using polar coordinates $x + iy = Qe^{i\psi}$, we find $\partial_t Q = -V'(Q) = Q_0 - Q$ where $V(Q) = Q(Q - 2Q_0)/2$ and $\partial_t\psi = 0$.

[c]When $Q_0 > 0$ there is also an unstable solution $\boldsymbol{Q} = 0$. When $Q_0 \le 0$, there is only a stable solution at $\boldsymbol{Q} = 0$, however $Q_0 < 0$ is unphysical in our case.

[d]It can however affect the knowledge we have of a system (57, 58).

Acknowledgments

The authors would like to thank K. Husain, D. Martin, and A. Murugan for helpful conversations.

Supplementary Material

Supplementary material is available at *PNAS Nexus* online.

Competing Interest

The authors declare no competing interests.

Funding

V.V. acknowledges support from the Army Research Office under grants no. W911NF-22-2-0109 and no. W911NF-23-1-0212, from the National Science Foundation under grant no. DMR-2118415 and from the Theory in Biology program of the Chan Zuckerberg Initiative. B.V.S. acknowledges support from a MRSEC-funded (NSF DMR-2011864) Kadanoff-Rice fellowship. M.F. and V.V. acknowledge support from the France Chicago center through a FACCTS grant. This work was completed in part with resources provided by the University of Chicago Research Computing Center. This research was partly supported by the National Science Foundation through the Physics Frontier Center for Living Systems (grant no. 2317138) and the National Institute for the Theory and Mathematics in Biology (NITMB).

Author Contributions

B.V.S., M.F., and V.V. contributed to the design of the study and writing of the manuscript. B.V.S. and M.F. performed analytical derivations. B.V.S. performed the numerical simulations.

Preprints

A preprint of this article is published at https://doi.org/10.48550/arXiv.2302.07402.

Data availability

The data underlying this article are available in a Zenodo repository, at https://doi.org/10.5281/zenodo.18904827.

References

1. Feynman RP. *Feynman lectures on computation: anniversary edition*. CRC Press, Boca Raton, FL, 2023.
2. Horowitz JM, Gingrich TR. 2020. Thermodynamic uncertainty relations constrain non-equilibrium fluctuations. *Nat Phys*. 16(1):15–20.
3. Landauer R. 1961. Irreversibility and heat generation in the computing process. *IBM J Res Dev*. 5(3):183–191.
4. O'Byrne J, Kafri Y, Tailleur J, van Wijland F. 2022. Time irreversibility in active matter, from micro to macro. *Nat Rev Phys*. 4(3):167–183.

Downloaded from academic.oup.com/pnasnexus/article/5/4/pgag077/8540115 by guest on 04 November 2026

5. Parrondo JMR, Horowitz JM, Sagawa T. 2015. Thermodynamics of information. *Nat Phys*. 11(2):131–139.
6. Ro S, *et al.* 2022. Model-free measurement of local entropy production and extractable work in active matter. *Phys Rev Lett*. 129(22):220601.
7. Braun M, Lansky Z, Hilitski F, Dogic Z, Diez S. 2016. Entropic forces drive contraction of cytoskeletal networks. *Bioessays*. 38(5):474–481.
8. Devereux HL, Turner MS. 2023. Environmental path-entropy and collective motion. *Phys Rev Lett*. 130(16):168201.
9. Doi M. *Soft matter physics*. OUP Oxford, 2013.
10. Hänggi P, Talkner P, Borkovec M. 1990. Reaction-rate theory: fifty years after Kramers. *Rev Mod Phys*. 62(2):251–341.
11. Israelachvili JN. *Intermolecular and surface forces*. Elsevier Science, 2011.
12. Reguera D, Rubí JM. 2001. Kinetic equations for diffusion in the presence of entropic barriers. *Phys Rev E*. 64(6):061106.
13. Wissner-Gross AD, Freer CE. 2013. Causal entropic forces. *Phys Rev Lett*. 110(16):168702.
14. Flory PJ, Rehner J. 1943. Statistical mechanics of cross-linked polymer networks I. Rubberlike elasticity. *J Chem Phys*. 11(11):512–520.
15. Bebon R, Robinson JF, Speck T. 2025. Thermodynamics of active matter: tracking dissipation across scales. *Phys Rev X*. 15:021050.
16. Brady JF. 2010. Particle motion driven by solute gradients with application to autonomous motion: continuum and colloidal perspectives. *J Fluid Mech*. 667:216–259.
17. Moran JL, Posner JD. 2017. Phoretic self-propulsion. *Annu Rev Fluid Mech*. 49(1):511–540.
18. Sabass B, Seifert U. 2012. Dynamics and efficiency of a self-propelled, diffusiophoretic swimmer. *J Chem Phys*. 136(6): 064508.
19. Sivak DA, du Buisson J, Bechhoefer J. 2024. Performance limits of information engines. *Adv Phys X*. 9(1):2352112.
20. Andrieux D, Gaspard P. 2008. Nonequilibrium generation of information in copolymerization processes. *Proc Natl Acad Sci U S A*. 105(28):9516–9521.
21. Binder PM, Danchin A. 2011. Life's demons: information and order in biology: what subcellular machines gather and process the information necessary to sustain life? *EMBO Rep*. 12(6):495–499.
22. Boël G, Danot O, de Lorenzo V, Danchin A. 2019. Omnipresent Maxwell's demons orchestrate information management in living cells. *Microb Biotechnol*. 12(2):210–242.
23. Charlesworth HJ, Turner MS. 2019. Intrinsically motivated collective motion. *Proc Natl Acad Sci U S A*. 116(31): 15362–15367.
24. Heins C, *et al.* 2024. Collective behavior from surprise minimization. *Proc Natl Acad Sci U S A*. 121(17):e2320239121.
25. Hopfer U. 2002. A Maxwell's demon type of membrane transport: possibility for active transport by abc-type transporters? *J Theor Biol*. 214(4):539–547.
26. Ito S, Sagawa T. 2015. Maxwell's demon in biochemical signal transduction with feedback loop. *Nat Commun*. 6(1):1–6.
27. Leff H, Rex AF. *Maxwell's demon 2 entropy, classical and quantum information, computing*. CRC Press, 2002.
28. Miller MB, Bassler BL. 2001. Quorum sensing in bacteria. *Ann Rev Microbiol*. 55(1):165–199.
29. Mizraji E. 2021. The biological Maxwell's demons: exploring ideas about the information processing in biological systems. *Theory Biosci*. 140(3):307–318.
30. Sachs G. 2005. Minimum shear wind strength required for dynamic soaring of albatrosses. *IBIS*. 147(1):1–10.
31. Sartori P, Granger L, Lee CF, Horowitz JM. 2014. Thermodynamic costs of information processing in sensory adaptation. *PLoS Comput Biol*. 10(12):e1003974.
32. Sartori P, Pigolotti S. 2015. Thermodynamics of error correction. *Phys Rev X*. 5(4):041039.
33. Stephens DW, Krebs JR. *Foraging theory*. In: *Foraging theory*. Princeton University Press, 2019.
34. Tu Y. 2008. The nonequilibrium mechanism for ultrasensitivity in a biological switch: sensing by Maxwell's demons. *Proc Natl Acad Sci U S A*. 105(33):11737–11741.
35. van Loon EE, Shamoun-Baranes J, Bouten W, Davis SL. 2011. Understanding soaring bird migration through interactions and decisions at the individual level. *J Theor Biol*. 270(1):112–126.
36. Dillavou S, Stern M, Liu AJ, Durian DJ. 2022. Demonstration of decentralized physics-driven learning. *Phys Rev Appl*. 18(1):014040.
37. Jung G, Ozawa M, Bertin E. 2025. Kinetic theory of decentralized learning for smart active matter. *Phys Rev Lett*. 134(24):248302.
38. Ziepke A, Maryshev I, Aranson IS, Frey E. 2022. Multi-scale organization in communicating active matter. *Nat Commun*. 13(1):6727.
39. Cichos F, Gustavsson K, Mehlig B, Volpe G. 2020. Machine learning for active matter. *Nat Mach Intell*. 2(2):94–103.
40. Demirörs AF, Akan MT, Poloni E, Studart AR. 2018. Active cargo transport with janus colloidal shuttles using electric and magnetic fields. *Soft Matter*. 14(23): 4741–4749.
41. Fernandez-Rodriguez MA, *et al.* 2020. Feedback-controlled active Brownian colloids with space-dependent rotational dynamics. *Nat Commun*. 11(1):4223.
42. Ghosh A, Fischer P. 2009. Controlled propulsion of artificial magnetic nanostructured propellers. *Nano Lett*. 9(6): 2243–2245.
43. Heuthe V-L, Panizon E, Gu H, Bechinger C. 2024. Counterfactual rewards promote collective transport using individually controlled swarm microrobots. *Sci Robot*. 9(97): eado5888.
44. Lavergne FA, Wendehenne H, Bäuerle T, Bechinger C. 2019. Group formation and cohesion of active particles with visual perception–dependent motility. *Science*. 364(6435): 70–74.
45. Muinos-Landin S, Fischer A, Holubec V, Cichos F. 2021. Reinforcement learning with artificial microswimmers. *Sci Robot*. 6(52):eabd9285.
46. Qian B, Montiel D, Bregulla A, Cichos F, Yang H. 2013. Harnessing thermal fluctuations for purposeful activities: the manipulation of single micro-swimmers by adaptive photon nudging. *Chem Sci*. 4(4):1420–1429.
47. Snezhko A, Aranson IS. 2011. Magnetic manipulation of self-assembled colloidal asters. *Nat Mater*. 10(9):698–703.
48. Tierno P, Golestanian R, Pagonabarraga I, Sagués F. 2008. Magnetically actuated colloidal microswimmers. *J Phys Chem B*. 112(51):16525–16528.

Downloaded from academic.oup.com/pnasnexus/article/5/4/pgag077/8540115 by guest on 04 November 2026

49. Wang X, Cichos F. 2024. Harnessing synthetic active particles for physical reservoir computing. *Nat Commun*. 15(1):774.
50. Yang Y, Bevan MA. 2018. Optimal navigation of self-propelled colloids. *ACS Nano*. 12(11):10712–10724.
51. Alvarez L, *et al.* 2021. Reconfigurable artificial microswimmers with internal feedback. *Nat Commun*. 12(1):4762.
52. Miskin MZ, *et al.* 2020. Electronically integrated, mass-manufactured, microscopic robots. *Nature*. 584(7822): 557–561.
53. Reynolds MF, *et al.* 2022. Microscopic robots with onboard digital control. *Sci Robot*. 7(70):eabq2296.
54. Huang C, Ding M, Xing X. 2020. Information swimmer: self-propulsion without energy dissipation. *Phys Rev Res*. 2(4): 043222.
55. Liu AT, *et al.* 2023. Colloidal robotics. *Nat Mater*. 22(12): 1453–1462.
56. Palagi S, Fischer P. 2018. Bioinspired microrobots. *Nat Rev Mater*. 3(6):113–124.
57. Gerbino F, Giachetti G, Le Doussal P, De Luca A. 2025. Measurement-induced phase transition in state estimation of chaotic systems and the directed polymer. *Phys Rev Res*. 7(3):1103/6375–8ncz.
58. Jin T, Martin DG. 2022. Kardar-Parisi-Zhang physics and phase transition in a classical single random walker under continuous measurement. *Phys Rev Lett*. 129(26):260603.
59. Pizzi A, Malz D, Nunnenkamp A, Knolle J. 2022. Bridging the gap between classical and quantum many-body information dynamics. *Phys Rev B*. 106(21):214303.
60. Pizzi A, Yao NY. 2024. Bipartite mutual information in classical many-body dynamics. *Phys Rev B*. 110(2):l020301.
61. Willsher J, Liu S-W, Moessner R, Knolle J. 2022. Measurement-induced phase transition in a chaotic classical many-body system. *Phys Rev B*. 106(2):024305.
62. Choi S, Bao Y, Qi X-L, Altman E. 2020. Quantum error correction in scrambling dynamics and measurement-induced phase transition. *Phys Rev Lett*. 125(3):030505.
63. Fisher MPA, Khemani V, Nahum A, Vijay S. 2023. Random quantum circuits. *Annu Rev Condens Matter Phys*. 14(Volume 14, 2023):335–379.
64. Skinner B, Ruhman J, Nahum A. 2019. Measurement-induced phase transitions in the dynamics of entanglement. *Phys Rev X*. 9(3):031009.
65. Maxwell C. 1871. Theory of Heat.
66. Plenio MB, Vitelli V. 2001. The physics of forgetting: Landauer's erasure principle and information theory. *Contemp Phys*. 42(1):25–60.
67. Szilard L. 1929. On the decrease of entropy in a thermodynamic system by the intervention of intelligent beings. *Z Phys*. 53(11):840–856.
68. Thomson W. 1874. Kinetic theory of the dissipation of energy. *Nature*. 9(232):441–444.
69. Chaté H, Solon A. 2024. Dynamic scaling of two-dimensional polar flocks. *Phys Rev Lett*. 132(26):268302.
70. Mahault B, Ginelli F, Chaté H. 2019. Quantitative assessment of the toner and TU theory of polar flocks. *Phys Rev Lett*. 123(21): 218001.
71. Cao FJ, Feito M. 2009. Thermodynamics of feedback controlled systems. *Phys Rev E*. 79(4):041118.
72. Esposito M, Van den Broeck C. 2011. Second law and Landauer principle far from equilibrium. *Europhys Lett*. 95(4): 40004.
73. Horowitz JM, Vaikuntanathan S. 2010. Nonequilibrium detailed fluctuation theorem for repeated discrete feedback. *Phys Rev E*. 82(6):061120.
74. Horowitz JM, Vaikuntanathan S. 2010. Nonequilibrium detailed fluctuation theorem for repeated discrete feedback. *Phys Rev E*. 82(6):061120.
75. Sagawa T, Ueda M. 2010. Generalized Jarzynski equality under nonequilibrium feedback control. *Phys Rev Lett*. 104(9):090602.
76. Cover TM, Thomas JA. *Elements of information theory*. Wiley-Interscience, 2006.
77. Cercignani C, Illner R, Pulvirenti M. *The mathematical theory of dilute gases*. Applied Mathematical Sciences, Springer, 1994.
78. Dorfman JR, van Beijeren H, Kirkpatrick TR. *Contemporary kinetic theory of matter*. Cambridge University Press, 2021.
79. Kardar M. *Statistical physics of particles*. Cambridge University Press, 2007.
80. Brilliantov NV, Pöschel T. *Kinetic theory of granular gases*. Oxford University Press on Demand, 2004.
81. Bertin E, Droz M, Grégoire G. 2006. Boltzmann and hydrodynamic description for self-propelled particles. *Phys Rev E*. 74(2):022101.
82. Attanasi A, *et al.* 2014. Information transfer and behavioural inertia in starling flocks. *Nat Phys*. 10(9):691–696.
83. Cavagna A, Giardina I, Ginelli F. 2013. Boundary information inflow enhances correlation in flocking. *Phys Rev Lett*. 110(16):168107.
84. Ferretti F, *et al.* 2022. Signatures of irreversibility in microscopic models of flocking. *Phys Rev E*. 106(3):034608.
85. Geiß D, Kroy K, Holubec V. 2022. Information conduction and convection in noiseless Vicsek flocks. *Phys Rev E*. 106(1):014609.
86. Ren J, Sun W, Manocha D, Li A, Jin X. 2018. Stable information transfer network facilitates the emergence of collective behavior of bird flocks. *Phys Rev E*. 98(5):052309.
87. Gaspard P. *The statistical mechanics of irreversible phenomena*. Cambridge University Press, 2022.
88. Schnakenberg J. 1976. Network theory of microscopic and macroscopic behavior of master equation systems. *Rev Mod Phys*. 48(4):571–585.
89. Bhatnagar PL, Gross EP, Krook M. 1954. A model for collision processes in gases. I. Small amplitude processes in charged and neutral one-component systems. *Phys Rev*. 94(3):511–525.
90. Farutin A, Misbah C. 2024. Singular bifurcations and regularization theory. *Phys Rev E*. 109(6):064218.
91. Kness M, Tuckerman LS, Barkley D. 1992. Symmetry-breaking bifurcations in one-dimensional excitable media. *Phys Rev A (Coll Park)*. 46(8):5054–5062.
92. Schulman J, Wolski F, Dhariwal P, Radford A, Klimov O. 2017. Proximal policy optimization algorithms. CoRR 06347v2. http://arxiv.org/abs/1707.06347v2, preprint: not peer reviewed.
93. Kirkwood JG. 1935. Statistical mechanics of fluid mixtures. *J Chem Phys*. 3(5):300–313.
94. Feynman RP, Leighton RB, Sands M. *The Feynman lectures on physics, Vol. I*. Basic Books, millennium edition, 2011.

Downloaded from academic.oup.com/pnasnexus/article/5/4/pgag077/8540115 by guest on 04 November 2026

95. Adachi K, Takasan K, Kawaguchi K. 2022. Activity-induced phase transition in a quantum many-body system. *Phys Rev Res*. 4(1):013194.
96. Antonov AP, Zheng Y, Liebchen B, Löwen H. 2025. Engineering active motion in quantum matter. *Phys Rev Res*. 7(3):033008.
97. Penner A-G, Viotti L, Fazio R, Arrachea L, von Oppen F. 2025. Heat-to-motion conversion for quantum active matter. *Phys Rev B*. 112(18):L180303.
98. Yamagishi M, Hatano N, Obuse H. 2024. Proposal of a quantum version of active particles via a nonunitary quantum walk. *Sci Rep*. 14(1):28648.
99. Anderson JA, Glaser J, Glotzer SC. 2020. HOOMD-blue: a python package for high-performance molecular dynamics and hard particle Monte Carlo simulations. *Comput Mater Sci*. 173:109363.
100. Weeks JD, Chandler D, Andersen HC. 1971. Role of repulsive forces in determining the equilibrium structure of simple liquids. *J Chem Phys*. 54(12):5237–5247.
101. Cercignani C. 1990. Are there more than five linearly-independent collision invariants for the Boltzmann equation? *J Stat Phys*. 58(5):817–823.
102. Sutton RS, Barto AG. *Reinforcement learning: an introduction*. 2nd ed. MIT Press, Cambridge, MA, 2018.

Downloaded from academic.oup.com/pnasnexus/article/5/4/pgag077/8540115 by guest on 04 November 2026